Space Weather®

Key Points:

- A sum of the first, third, and fifth sine harmonics is used to approximate equatorial electron Pitch angle distributions (PADs) measured by the MagEIS detector onboard the Van Allen Probes
- We present a PAD model with a continuous dependence on L, magnetic local time and activity, driven by the solar wind dynamic pressure
- The model allows reconstructions of equatorial PADs from uni- and omni-directional measurements at off-equatorial latitudes

An Empirical Model of the Equatorial Electron Pitch Angle Distributions in Earth's Outer Radiation Belt

Artem Smirnov[1,2] ⓘ, Yuri Y. Shprits[1,2,3] ⓘ, Hayley Allison[1] ⓘ, Nikita Aseev[1,2] ⓘ, Alexander Drozdov[3] ⓘ, Peter Kollmann[4] ⓘ, Dedong Wang[1] ⓘ, and Anthony Saikin[3] ⓘ

[1]Helmholtz Centre Potsdam GFZ German Research Centre for Geosciences, Potsdam, Germany, [2]Institute of Physics and Astronomy, University of Potsdam, Potsdam, Germany, [3]Department of Earth, Planetary and Space Sciences, University of California, Los Angeles, CA, USA, [4]Applied Physics Laboratory, Johns Hopkins University, Laurel, MD, USA

Abstract In this study, we present an empirical model of the equatorial electron pitch angle distributions (PADs) in the outer radiation belt based on the full data set collected by the Magnetic Electron Ion Spectrometer (MagEIS) instrument onboard the Van Allen Probes in 2012–2019. The PADs are fitted with a combination of the first, third and fifth sine harmonics. The resulting equation resolves all PAD types found in the outer radiation belt (pancake, flat-top, butterfly and cap PADs) and can be analytically integrated to derive omnidirectional flux. We introduce a two-step modeling procedure that for the first time ensures a continuous dependence on L, magnetic local time and activity, parametrized by the solar wind dynamic pressure. We propose two methods to reconstruct equatorial electron flux using the model. The first approach requires two uni-directional flux observations and is applicable to low-PA data. The second method can be used to reconstruct the full equatorial PADs from a single uni- or omnidirectional measurement at off-equatorial latitudes. The model can be used for converting the long-term data sets of electron fluxes to phase space density in terms of adiabatic invariants, for physics-based modeling in the form of boundary conditions, and for data assimilation purposes.

Plain Language Summary Pitch angle distributions (PADs) are critically important for understanding the dynamics of trapped electrons in Earth's radiation belt region. Specific PAD types are linked to processes acting within the radiation belts which relate to the origins and loss mechanisms of the particle populations, as well as wave activity. In this study we present a polynomial model of the equatorial electron PADs at energies 30 keV–1.6 MeV with a continuous dependence on L-shell, magnetic local time and activity driven by the solar wind dynamic pressure. The model can be used to reconstruct equatorial electron flux from observations at high latitudes and can be applied for converting the long-term electron flux data sets to phase space density, driving the boundary conditions for the physics-based simulations and for data assimilation.

1. Introduction

The Van Allen radiation belts contain charged energetic particles, primarily protons and electrons, trapped by the terrestrial magnetic field. Electron radiation belts exhibit a dual-zone structure, consisting of the inner and outer belts (e.g., Van Allen & Frank, 1959). The two belts are separated by the slot region which is usually devoid of electrons but can be filled during geomagnetically active times (e.g., Reeves et al., 2016). Charged particles that move much faster than the bulk motion of the plasma organize very well relative to the magnetic field, so that measurements over the full sky are not needed. This is generally the case for electrons. Particle detectors on spinning satellites can sweep through all angles to the magnetic field, measuring intensities for local pitch angle bins. The resulting angular distributions, referred to as the pitch angle distributions (PADs), play an important role in understanding trapped electrons' dynamics in the radiation belt region. In particular, specific PAD shapes are linked to distinct processes that relate to the origins of these electrons, their loss mechanisms, and wave activity (e.g., Horne et al., 2003; Lyons et al., 1972; Ni et al., 2015; Roederer, 1967; Walt, 2005; West et al., 1973).

Several PAD types have been identified in the radiation belt region (e.g., West et al., 1973). Some of the most common types include pancake, butterfly, flat-top, and cap PADs. The pancake distribution, also known as the normal PAD, exhibits a maximum flux value around 90° pitch angle (PA), which smoothly decreases toward lower PAs. It is considered to be the most frequently observed PAD type in the inner magnetosphere, especially on the dayside (e.g., Gannon et al., 2007), and generally results from the particle pitch angle diffusion and loss

of the field-aligned electrons to the atmosphere. The PADs that exhibit a maximum flux at around 30°–60° PA with a relative deficit of the 90° electrons are called butterfly distributions (e.g., West et al., 1973). The quiet-time butterflies in the outer belt are prevalent at high L-shells on the night side and mainly formed as a result of drift shell splitting (e.g., Selesnick & Blake, 2002). They can also be caused by wave activity in the outer radiation belt (e.g., Artemyev et al., 2015; Kamiya et al., 2018) and in the inner zone (e.g., Albert et al., 2016). Another common PAD type, a flat-top PAD, has a relatively isotropic flux around 90° PA. Horne et al. (2003) showed it to be a transition shape between the butterfly and pancake PADs. The cap (or head-and-shoulders) PAD shape manifests as a pancake with an additional peak in flux close to 90° PA. It has been shown to form due to interactions with the plasmaspheric hiss waves which scatter the near equatorially mirroring electrons slower than those at lower pitch angles (e.g., Lyons et al., 1972).

Particles trapped in the terrestrial magnetosphere experience a bounce motion between the two mirror points (e.g., Roederer & Zhang, 2016). At the geomagnetic equator, every bouncing particle can be observed, whereas at an off-equatorial magnetic latitude the satellite cannot sample the below-mirroring particles and resolves only a part of the equatorial PAD. Therefore, the most complete information about electron PADs can be obtained through measurements in close proximity to the geomagnetic equator (e.g., Chen et al., 2014). However, many satellites operate at non-equatorial orbits, for instance the Low Earth Orbit (LEO), where the range of observed equatorial pitch angles in the outer belt is limited to small PAs (less than several degrees). In recent years, there has been an increasing interest in using LEO data for radiation belt monitoring (e.g., Allison et al., 2018; Claudepierre & O'Brien, 2020; Green et al., 2021; Reidy et al., 2021). In particular, the Polar Operational Environmental Satellites and Meteorological Operational Satellites missions provide long-term data sets that can be used for radiation belt modeling in the form of boundary conditions and for data assimilation. Both constellations provide observations of only a narrow range of pitch angles by two detectors pointing in vertical and horizontal directions, and in order to reconstruct the full equatorial PADs it is necessary to employ appropriate pitch angle models. In addition, several long-term missions, including Global Positioning System (GPS), Cluster, etc. Measure omnidirectional electron flux and do not provide pitch angle-dependent distributions. In order to convert these long-term data sets to phase space density in terms of adiabatic invariants, it is necessary to have a reliable model of the PADs.

In a companion paper, Smirnov et al. (2022b) analyzed the storm-time evolution of equatorial electron PADs at energies 30 keV–1.6 MeV. The authors performed a superposed epoch analysis of 129 strong geomagnetic storms in 2012–2019 and examined the morphology of electron PADs in the outer radiation belt for day and night magnetic local times (MLTs). It was shown that for energies >150 keV, the PADs undergo significant systematic changes during geomagnetic storms. In this paper, we aim to generalize this dependence on activity by creating an empirical polynomial model of the equatorial electron PADs. Previous PAD models binned the data into several activity intervals based on the Dst (Chen et al., 2014), AE (Zhao et al., 2018) and Kp (Allison et al., 2018; Zhao et al., 2021) indices, as well as into spatial bins in L-MLT coordinates. In this study, we use the solar wind dynamic pressure as a driving parameter and employ a 2-step modeling procedure (described in Section 3) which provides a continuous dependence on L, MLT and activity for the first time. Furthermore, our model can be applied to reconstruct the full equatorial PADs from both uni- and omnidirectional observations at off-equatorial latitudes by using the selected parameterization technique.

The paper is divided into six parts. Section 2 describes the data and methodology used in this study. Section 3 is devoted to model construction. In Section 4 we introduce two methods to reconstruct equatorial flux from observations at off-equatorial latitudes and show the model validation. The results are discussed in Section 5, and the conclusions are presented in the final section.

2. Data Set and Methodology

2.1. Data Set

The Van Allen Probes mission, initially called the Radiation Belt Storm Probes (RBSP), operated in 2012–2019 and consisted of two identical spacecraft (probes A and B) following a highly elliptical medium Earth orbit (MEO) with an apogee of ~620 km, a perigee of around 30,400 km and an orbital period of 9 hr (e.g., Mauk et al., 2012). The probes were spinning with a period of around 11s (e.g., Claudepierre et al., 2021). Van Allen Probes covered L-shells from 1.2 to ~5.8 on the dayside and ~6.2 on the nightside and revolved in MLT covering all magnetic local times every ~22 months (e.g., Mauk et al., 2012). Onboard, the Magnetic Electron Ion

Spectrometer (MagEIS) instruments measured intensities of trapped electrons and ions (e.g., Blake et al., 2013). Each Probe had four MagEIS units providing excellent coverage in energies and pitch angles (e.g., Claudepierre et al., 2021). MagEIS maintained a quasi-constant magnetic field inside the instrument chamber, which allowed to separate the incoming electrons and protons (for details, see Blake et al., 2013). Furthermore, using the constant magnetic field created a separation between electrons of different energies which hit different detector pixels numbered according to energy (see e.g., Figure 1 in Claudepierre et al., 2021).

This study employs MagEIS pitch angle-resolved electron flux data (level 3) at energies 30 keV–~1.65 MeV during Van Allen Probes' entire lifespan in 2012–2019. For each moment in time and each local pitch angle, we computed the corresponding equatorial PA using the relation $\alpha_{eq} = \arcsin\left(\sqrt{\frac{B_{eq}}{B_{loc}}}\sin(\alpha_{loc})\right)$, where B_{loc} and B_{eq} represent the values of the local and equatorial magnetic field, respectively, corresponding to the magnetic field line at the satellite location. The magnetic field magnitude and the McIlwain L parameter (Lm) were calculated using the TS04D storm-time model (Tsyganenko & Sitnov, 2005). The data from October 2012 until October 2018 are used for model construction, and the subsequent seven months of data (toward the end of the mission) are reserved for validation. The data are averaged by five minutes with an assumed symmetry with respect to 90° PA, and the PADs which had no data points at high (>75°) or low (<25°) equatorial pitch angles were removed in order to exclude unphysical shapes. Electron flux values in the slot region can often be at background values and the corresponding PADs are less indicative of the physics. In order to remove the background, we exclude PADs where the maximum value of electron flux is lower than 20 keV^{-1} cm^{-2}s^{-1}sr^{-1}. This value was empirically selected to filter out PAD shapes corresponding to background for energies up to 1.65 MeV. Using higher threshold values led to the removal of realistic PAD shapes and limited the statistics for model fitting at low L-shells.

2.2. PAD Approximation Using Sine Series

In order to create a PAD model, it is crucial to approximate PADs with a trigonometric function that can fit all PAD types. In previous studies, PADs have been approximated by the $\sin^n \alpha$ function, where the power n shows the steepness of the distributions (see e.g., Gannon et al., 2007, Vampola, 1998, etc.). This parametrization resolves the pancake, flat-top, isotropic and field-aligned PADs. However, it cannot capture the head-and-shoulders distributions which are frequently observed at low energies, as well as the butterfly PADs which account for up to 80% of all PADs at high L-shells on the nightside (e.g., Ni et al., 2016). Allison et al. (2018) used a combination of two $\sin^n \alpha$ terms which helped to resolve cap but not butterfly PADs. Several studies have employed Legendre polynomials to approximate electron PADs in the Earth's radiation belts (e.g., Chen et al., 2014; Zhao et al., 2018, 2021). In particular, Chen et al. (2014) created the first PAD model in the outer belt, and Zhao et al. (2018) extended this methodology to both inner and outer zones and showed that PADs in the outer belt could be approximated by the first three even terms of the Legendre series expansion, while it was necessary to include higher harmonics at $L < 3$ due to the larger loss cones and generally steeper PAD shapes.

In order to approximate the equatorial electron PADs, we use a sine series expansion of the form:

$$j(\alpha) = A_0 + A_1 \sin \alpha + A_3 \sin 3\alpha + A_5 \sin 5\alpha, \tag{1}$$

where j is electron flux as a function of PA α. Having electron flux observations at several pitch angles, we use least-squares fitting to obtain the coefficients A_0, A_1, A_3, and A_5. The Fourier sine series expansion has been used by Clark et al. (2014) to analyze PADs in Saturn's radiation belts. Smirnov et al. (2022b) used this approximation for the first time to analyze the storm-time dynamics of electron PADs in the Earth's outer radiation belt. The Fourier expansion has notable advantages, for instance, expression (1) can be analytically integrated over the solid angle and the fitted PADs can be converted to omnidirectional flux.

Figure 1a demonstrates the shape functions for the first five sine harmonics. The even harmonics ($\sin 2\alpha$ and $\sin 4\alpha$) are asymmetric with respect to 90° PA and therefore are omitted and only odd terms are used further on. From Figure 1(a) it can be seen that generally, the first Fourier component ($\sin \alpha$) resembles the pancake PAD shape (shown in Figure 1b), corresponding to large values of the A1 coefficient and small values of A3 and A5 coefficients. The coefficient before $\sin 3\alpha$ demonstrates the contribution of the butterfly shape. Indeed, the $\sin(3\alpha)$ function exhibits a double peak at around 30° and 150° PA and has a minimum at 90°. Combined with the $\sin \alpha$ term, it can well approximate the butterfly distributions (Figure 1(c)). An example of the cap distribution
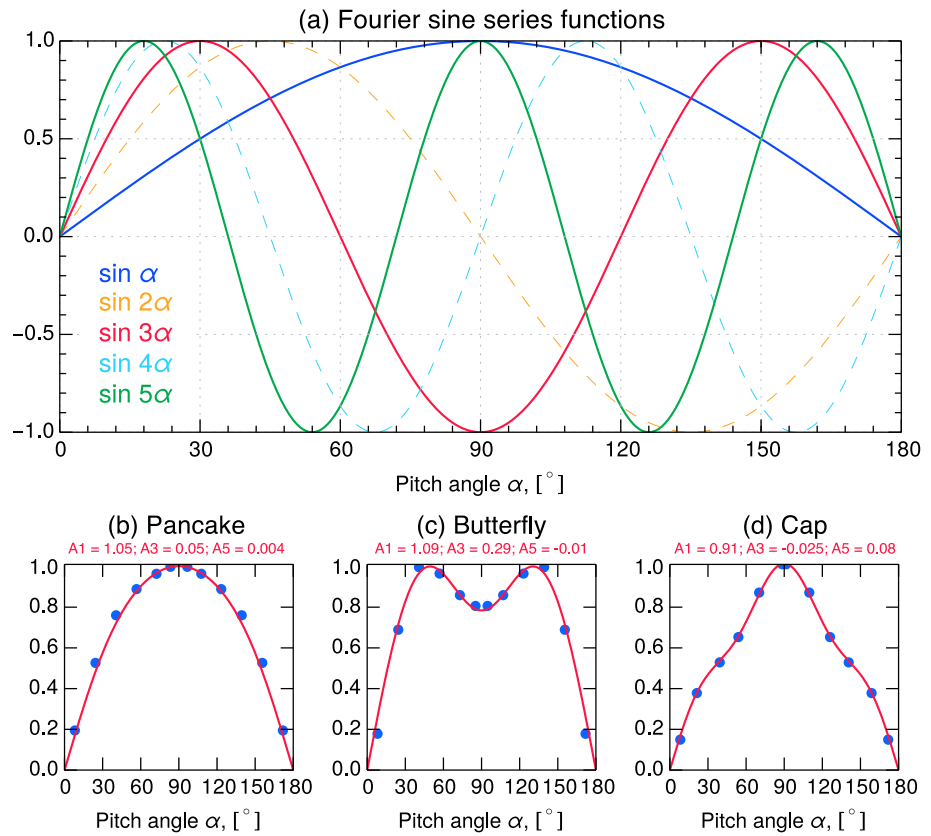
Figure 1. (a) Fourier sine functions up to degree 5 (b, c, d); examples of the fitted pancake, butterfly and cap equatorial pitch angle distributions, respectively, normalized using Equation (2). Blue dots show the normalized Magnetic Electron Ion Spectrometer observations and the red lines give the fitted shapes.

is demonstrated in Figure 1(d). In order to fit this shape, a combination of the first and fifth Fourier harmonics is needed, since the first term, reflected in the A1 value, gives the general pancake shape and the fifth term (A5) introduces the head-and-shoulders structure due to the two depletions in the $\sin 5\alpha$ shape around 45° and 135° PA and an additional bump around 90° PA. It is worth noting that in butterfly distributions the A3 coefficient can increase to relatively large values (up to 0.7), while only small positive A5 values (0.05–0.15) are sufficient to fit the head-and-shoulders PAD shape. As can be seen from Figure 1, the Fourier sine series expansion well resolves all main types (pancake, butterfly and cap) of equatorial PADs found in the outer belt. The PAD shapes resulting from various combinations of the A1, A3 and A5 coefficients are demonstrated in the companion study (Smirnov et al. (2022b), Figure 2). We note that it is possible to extend this methodology to lower L-shells and resolve the steeper PAD shapes observed there by adding the higherorder terms to Equation (1), similar to the models based on Legendre polynomials (Zhao et al., 2018, 2021).

In Equation (1), the A_0 coefficient represents the value of electron flux in the edge of the loss cone, which corresponds to the minimum flux value for the respective PAD. For each of the PADs, one can also find the maximum flux value defined as $j_{\max} = \max_{\alpha_{eq} \in (0,90)} j(\alpha_{eq})$. In this study, we are most interested in the PAD shapes. In Section 3 we therefore normalize the PADs and develop a model for the normalized shapes, and later present a method to reconstruct absolute values of electron flux with the help of observations. Before proceeding with analyzing the pitch angle shapes, every PAD is normalized as follows. At first, we fit the said PAD to Equation (1) and obtain the $A_{0,1,3,5}$ coefficients. After that, the PAD $j(\alpha)$ is evaluated with a very small pitch angle step of 0.01°, and the maximum flux value $j_{\max}$ is empirically found. The odd coefficients $A_{1,3,5}$ are normalized to the minimum ($A0$) and maximum ($j_{\max}$) values so that each individual PAD spans from 0 to 1 using the equation:

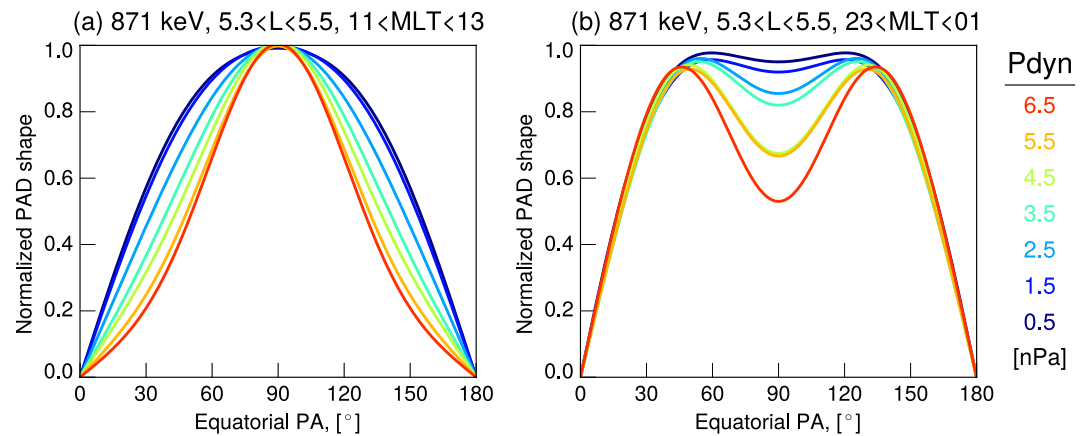$$\tilde{A}_i = \frac{A_i}{j_{\max} - A_0}, i = \{1, 3, 5\}, \tag{2}$$

Figure 2. Averaged pitch angle distribution shapes of 871 keV electrons measured by the Magnetic Electron Ion Spectrometer instrument at L ∼ 5.4 on the dayside (a) and on the nightside (b) for different values of the solar wind dynamic pressure ($\pm$0.25 nPa).

where $\tilde{A}_i$ denotes the normalized value of the respective coefficient A_i. In order to remove low-quality PAD fits, we use a criterion proposed by Carbary et al. (2011) which uses the standard deviation of the difference between the measured and fitted flux normalized to the minimum and maximum values ($\sigma_N = \sigma/(j_{max} - A_0)$). The good quality fits correspond to σ_N values below 0.2, while PADs with $\sigma_N > 0.2$ represent low-quality fits and were not used in the model construction. The details on this quality flag and examples of high- and low-quality fits are given in Smirnov et al. (2022b) (e.g., their Figure S1 in the Supporting Information S1).

It should be noted that the PADs normalized by Equation (2) do not carry information about the flux levels and should only reflect the shapes of the distributions. In the companion paper, Smirnov et al. (2022b) analyzed the storm-time evolution of electron PADs in terms of the normalized shapes. In the present study, we, first, create a model of the normalized PADs driven by the solar wind dynamic pressure (Section 3). Furthermore, in Section 4 we give two methods of reconstructing electron flux from the model by using off-equatorial observations.

3. Model Construction

Pitch angle distributions in the outer radiation belt are known to be very dynamic (e.g., Horne et al., 2003; Gu et al., 2011). It is therefore crucial to select a suitable driving parameter for the model. In a companion study, Smirnov et al. (2022b) analyzed the storm-time evolution of the PAD shapes normalized using the methodology described above. It was found that at energies >150 keV, PADs undergo a systematic evolution during geomagnetic storms. Furthermore, the main processes governing the PAD dynamics in the outer belt can be attributed to changes in the solar wind dynamic pressure (for details, see Smirnov et al., 2022b). In Figure 2, we demonstrate averaged PAD shapes of 871 keV electrons observed by MagEIS at L ∼5.4 for the day- and nighttime MLTs, colored by the values of the solar wind dynamic pressure. It can be seen that on the dayside, the distributions are of pancake shape and that their 90°-anisotropy increases with Pdyn, likely due to the magnetic field compression. On the nightside, the distributions have butterfly shapes, and the 90°-minima become more pronounced with increasing SW pressure, due to the more intense drift shell splitting (for details, see Smirnov et al. (2022b)). From Figure 2 one can see that the PAD shapes exhibit a strong dependence on dynamic pressure, which is analyzed in more detail below. Furthermore, Smirnov et al. (2022b) showed that the morphology and response to activity of electron PADs is strongly dependent on energy. Therefore, the model presented here is constructed for each energy channel.

We first examine the normalized occurrence plots of the PAD shape coefficients $A_{1,3,5}$ within a chosen range of L and MLT with respect to solar wind dynamic pressure, which are constructed as follows. At first, the predictor variable (on the x-axis) is divided into 20 bins. Then, for each interval of the x-axis, the corresponding A_i coefficients are also split into the same number of bins. For each bin, the number of occurrences is calculated and then divided by the total number of points in the respective x-interval. Such a representation effectively demonstrates how the PAD coefficients are distributed for each bin of the predictor variable and essentially
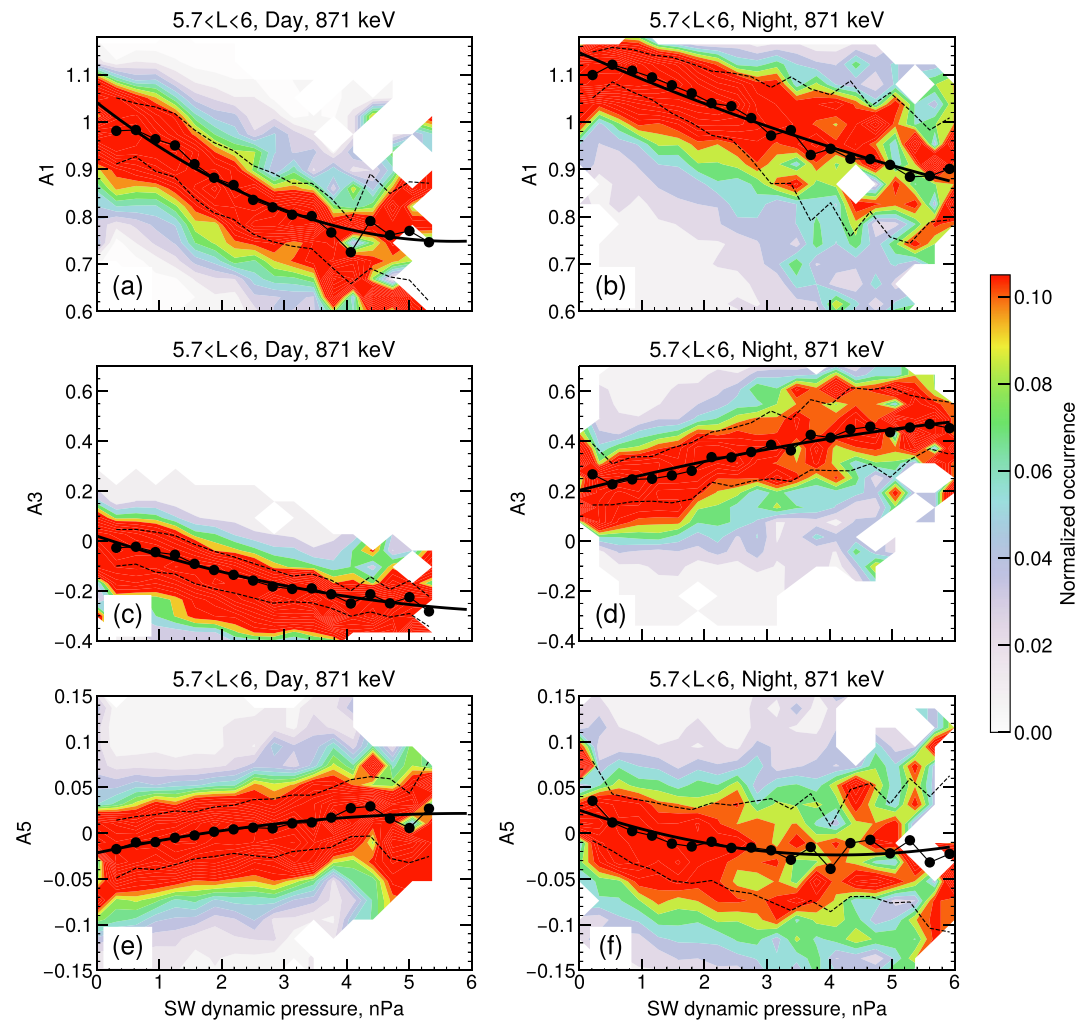
Figure 3. Normalized occurrence plots of the A_1, A_3 and A_5 coefficients as a function of solar wind dynamic pressure for 871 keV electrons at day side magnetic local time (MLT) (a,c,e) and night side MLT (b,d,f), respectively. The median values of the Fourier coefficients in each bin of dynamic pressure are shown as black dots, and the dashed lines give the interquartile range. The bold black lines show the quadratic trends fitted to the medians using Equation (3). The contour function was applied to the plot. Pitch angle distributions for the median values of parameters shown here can be found in Figure 2.

represents a normalized 2D probability distribution function (e.g., Kellerman & Shprits, 2012). In particular, it is well-established that throughout the Van Allen Probes era most of the points were attributed to the quiet conditions, and storm-time events, especially the strong ones, were rare. By normalizing the coefficient values to their respective activity bin, a more balanced estimation of the distributions can be obtained.

In Figure 3, we show the normalized occurrence histograms for the day- and night MLTs at high L-values (from 5.7 to 6) of 871 keV electrons. It can be seen in Figure 3(a) that on the dayside, the pancake coefficient A1 decreases with increasing Pdyn, from ~1 at low pressure to ~0.75 under dynamic pressure of 6 nPa. Furthermore, the butterfly coefficient A3 also decreases, from 0 at low Pdyn values to < −0.2 at higher Pdyn (Figure 3c). The cap coefficient A5, while increasing slightly for higher Pdyn, remains very small and is generally close to 0. These results agree very well with the superposed epoch analysis presented in (Smirnov et al., 2022b). The simultaneous decrease in A1 and A3 coefficients with Pdyn at L > 5.7 (see e.g., Figure 3d in Smirnov et al., 2022b) corresponds to more anisotropic PADs during the storm's main phase as a result of the geomagnetic field compression. On the night side, the pancake coefficient decreases from >1.1 to around 0.9 with increasing Pdyn (Figure 3b), while the contribution of the butterfly coefficient A3 roughly doubles with higher Pdyn, which also agrees with the findings of Smirnov et al., 2022b. As the stronger dynamic pressure compresses the Earth's magnetosphere, the effect of drift shell splitting becomes more evident. One notable feature in Figure 3(b) is that

the spread of A1 values increases with Pdyn. This indicates that while there is a clear dependence of the PAD coefficients on dynamic pressure, the storm times correspond to complex processes in the outer radiation belt (Reeves et al., 2003), which might not be captured by a simple empirical relation to Pdyn. It is of note that the Pdyn values generally lie from 0 to 6 nPa but can also experience spikes of up to 50 nPa. In Figure S1 in Supporting Information S1, we show that over 97% of values are below 5.5 nPa and therefore the model statistics for the spikes would be limited. Thus, all values corresponding to Pdyn >5.5 nPa are combined into a separate model bin which corresponds to intervals of very high activity.

The black dots in Figure 3 indicate the median coefficient values for each interval of the dynamic pressure. It can be seen that the general dependence can be well approximated using the quadratic trend line of the form:

$$A_{1,3,5}(\text{Pdyn}) = c_0 \cdot \text{Pdyn}^2 + c_1 \cdot \text{Pdyn} + c_2, \tag{3}$$

where Pdyn denotes the solar wind dynamic pressure. We divide data into spatial bins using a step of 1 hr MLT and 0.2 L, and in order to achieve better statistics we add data points from within ±3h MLT and ±0.15 L-shell to each of the bins, which is equivalent to smoothing in L and MLT dimensions. At L>5.8, the step in L was increased to ±0.25 L due to the limited Van Allen Probes statistics at high L-shells. By fitting the medians of each of the Fourier coefficients to the dynamic pressure using Equation 3, we obtain matrices of the quadratic trend coefficients $c_{0,1,2}$ as functions of L and MLT. It is now necessary to introduce a continuous dependence on L and MLT into the model.

In order to avoid a discontinuity at the 24-00 MLT boundary, it is common practice to replace MLT with its sine and cosine values, denoted as cMLT = cos $(2\pi \cdot \text{MLT}/24)$, and sMLT = sin $(2\pi \cdot \text{MLT}/24)$ (see, e.g., Bortnik et al., 2016; Katsavrias et al., 2021). Then, the matrix of the trend coefficients c_i is fitted to L, sMLT and cMLT using the equation:

$$c_{0,1,2}(L, cMLT, sMLT) = \sum_{i=0}^{N} \sum_{j=0}^{N} \sum_{\substack{k=0 \\ i+j+k \leq N}}^{N} \left(p_{ijk} \cdot L^i \cdot cMLT^j \cdot sMLT^k \right), \tag{4}$$

where N is the degree of the polynomial. In this study we use an empirically selected value of $N = 7$. Including higher orders made the results oscillatory, while the polynomials of order less than 7 were missing features seen in the data. The values of p_{ijk} are obtained using Theil-Sen regression which is a modification of the multivariate linear regression robust to outliers (Sen, 1968; Theil, 1950). The final model is a collection of the p_{ijk} coefficients, and from these the initial Fourier coefficients $A_{1,3,5}$ can be obtained through the script provided in Smirnov et al. (2022a).

Figure 4 shows a comparison between the values of PAD coefficients predicted by the polynomial model and those averaged for the MagEIS data under dynamic pressure values of ~3 nPa (from 2.8 to 3.2 nPa). It can be seen that for all three coefficients, the model values are in very good agreement with data averages. Several regions can be qualitatively defined in Figure 4. For instance, one can observe lowered values of A1 and A3 coefficients on the dayside at L > 5, which corresponds to steep pancake distributions. At high L-values on the nightside, on the other hand, there is an increase in the A3 coefficient, which corresponds to the butterfly distributions resulting from the drift shell splitting and magnetopause shadowing. At $L \sim 5$, the butterfly coefficients A3 decrease to zero, and the corresponding PADs are of pancake type. This is in line with theoretical predictions by Roederer (1967), who showed that drift shell splitting is only effective at $L > 5$. One interesting feature in Figure 4(c) is the increase in the butterfly coefficient A3 on the dayside at low L-values, which manifests as a band around 12:00 MLT but is slightly shifted toward the dawn. These L-shells correspond to the slot region for the 735 keV electrons, and the existence of these butterfly distributions has previously been attributed to the wave activity (e.g., Albert et al., 2016). In Figure S2 in Supporting Information S1, we demonstrate the same comparison for Pdyn values of 0.5 nPa, corresponding to the quiet times, and Pdyn~5 nPa corresponding to the storm times. The values of the PAD coefficients are in good agreement with MagEIS observations both for quiet and active conditions, and the observed PAD morphology and activity dependence is in line with previous results based on the superposed epoch analysis presented in Smirnov et al. (2022b). In Figure S4 in Supporting Information S1 it is also demonstrated that observed and modeled PAD shapes are in good agreement for several satellite orbits during different phases of geomagnetic storms. Moreover, Figure S5 in Supporting Information S1 shows the modeled PAD coefficients under low and high (0.6 and 6 nPa, respectively) values of dynamic pressure both
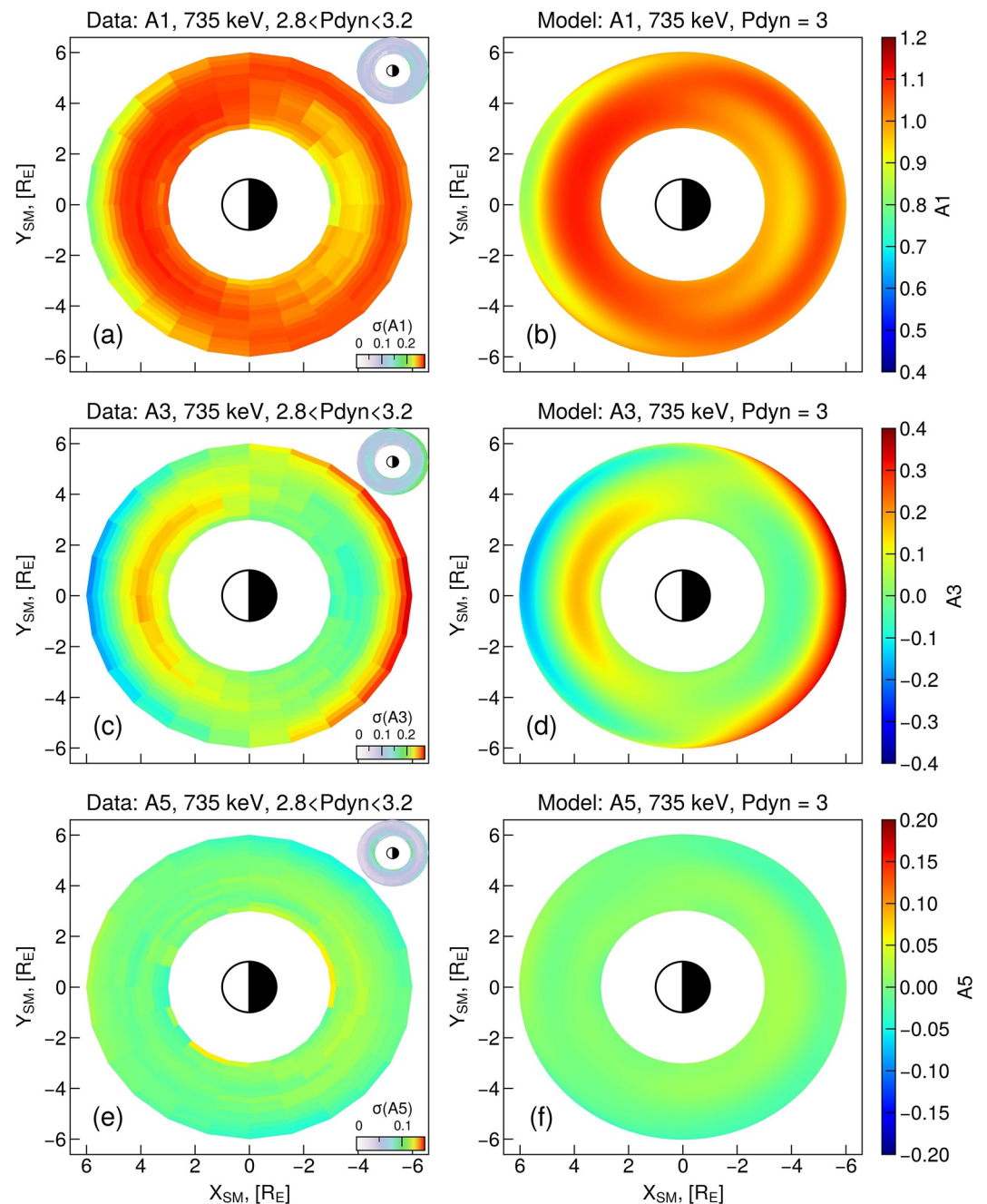
Figure 4. A comparison between the median pitch angle coefficients A1, A3 and A5 from Magnetic Electron Ion Spectrometer data (panels a,c,e, respectively) and their model values (panels b,d,f). The inset plots in panels (a,c,e) show the standard deviations of the respective coefficients. The values shown here are for 735 keV electrons and Pdyn~3 nPa.

for day and night MLTs as a function of energy. It can be seen that the values of the PAD coefficients in Figure S5 agree well with the previous study by Smirnov et al. (2022b) which investigated the storm-time PAD evolution and therefore the model depicts the main features of the PAD dynamics across different energies.

The model constructed here describes the pitch angle distribution shapes for $L = 3$–6 at energies from ~30 keV up to ~1.65 MeV. The model is continuous with respect to L and MLT. Furthermore, the developed model is the first PAD model to have a continuous dependence on activity, in this study parametrized by the solar wind dynamic pressure. It has been established that the model captures the main effects seen throughout the storm-time evolution of PADs. The model presented in the current Section gives the normalized PAD shapes. In order to apply the

model to the data one needs to be able to connect the PAD shapes to the flux intensities, and the two methods to recover this information are described in the following Section.

4. Model Validation

4.1. Reconstructing Equatorial PADs Using Two Flux Measurements at Low Pitch Angles

In this section, we describe the reconstruction of the full equatorial PADs using the developed model and 2 directional observations of electron flux at low PAs. From Equations (1) and (2) it is evident that after normalizing the PAD shapes, one needs to retrieve 2 parameters to relate the PAD shapes back to flux magnitudes, namely the A0 coefficient and the scaling factor equal to maximum flux (j_{max}) minus A0. In this case, having two observations allows for an estimation of these parameters using the following procedure.

At each of the two known equatorial pitch angles α_1 and α_2, we can re-write Equation (1) in the form:

$$j_{\text{data}}(\alpha_i) = A_0 + A_1 \sin \alpha_i + A_3 \sin 3\alpha_i + A_5 \sin 5\alpha_i, \tag{5}$$

with $i = \{1, 2\}$, and for the same equatorial pitch angles, the normalized PAD shapes calculated using the developed model can be expressed as follows:

$$j_{\text{model}}(\alpha_i) = \tilde{A}_1 \sin \alpha_i + \tilde{A}_3 \sin 3\alpha_i + \tilde{A}_5 \sin 5\alpha_i. \tag{6}$$

Therefore, one can write:

$$j_{\text{data}}(\alpha_i) = s \cdot j_{\text{model}}(\alpha_i) + A_0, \tag{7}$$

where $s = j_{\text{max}} - A_0$ is the scaling factor. It can be retrieved by dividing the difference between the observed fluxes at two pitch angles to that calculated from the model. Then, the A0 value can be obtained by substituting values into Equation (7) for either of the data points. After both of the parameters have been calculated, the full equatorial PAD can be reconstructed.

Figure 5 shows the validation of the modeled electron flux by the RBSP observations for 1.08 MeV MagEIS channel. In Figure 5(a), electron flux evaluated from RBSP observations at a high equatorial PA of 80° is given. Each of the observed MagEIS PADs was propagated to 80° by using the fit to Equation 1. In panel (b) we show electron flux reconstructed using the method described above. We first compute the "observed" flux at 8° and 17° PA (i.e., the two lowest MagEIS pitch angles). Then, these values are supplied as inputs and using the method described above the flux at 80° equatorial PA is retrieved. It can be seen that the observed and reconstructed fluxes are highly consistent, which shows the capacity of the model to reproduce equatorial PADs from low pitch angle data. The logarithmic difference between the observed and reconstructed flux is shown in panel (c). The logarithmic difference mostly shows values within ±0.25, although at a relatively small number of points there can be an underestimation on the order of 1. These outliers mainly occur following the spikes of the dynamic pressure, in particular, when the Pdyn values decrease but the Kp index remains at elevated levels. This indicates that the model could benefit from including time-history of solar wind parameters and geomagnetic indices, which can be a topic of a future study. Furthermore, there is slight overestimation of electron flux in the slot region (Figure 5(c)), which appears to be relatively independent of activity. This is likely due to the fact that the flux in the slot region is often at background levels and therefore there are fewer data points for the model fitting. Nevertheless, the mean logarithmic difference at $L < 4$ equals −0.13, which is considered acceptable for radiation belts modeling.

It is also crucial to establish whether the model presented in this paper performs better than a simple approximation of the form $j(\alpha) = A_n \sin(\alpha)$. To retrieve electron flux at 80° equatorial PA using this approximation, we use MagEIS electron flux evaluated at a low pitch angle of 12.5° and obtain the A_n value. In Figure 5(d) we show the flux propagated using the $\sin(\alpha)$ approach. It is apparent that electron flux is overestimated compared to observations shown in panel (a). The logarithmic difference shown in Figure 5(e) is much larger than that computed for the Fourier-coefficients-based model. Indeed, while in panel (c) the logarithmic difference was close to 0 throughout the test interval, in panel (e) the values are in general of the order of −0.5. In order to quantify the
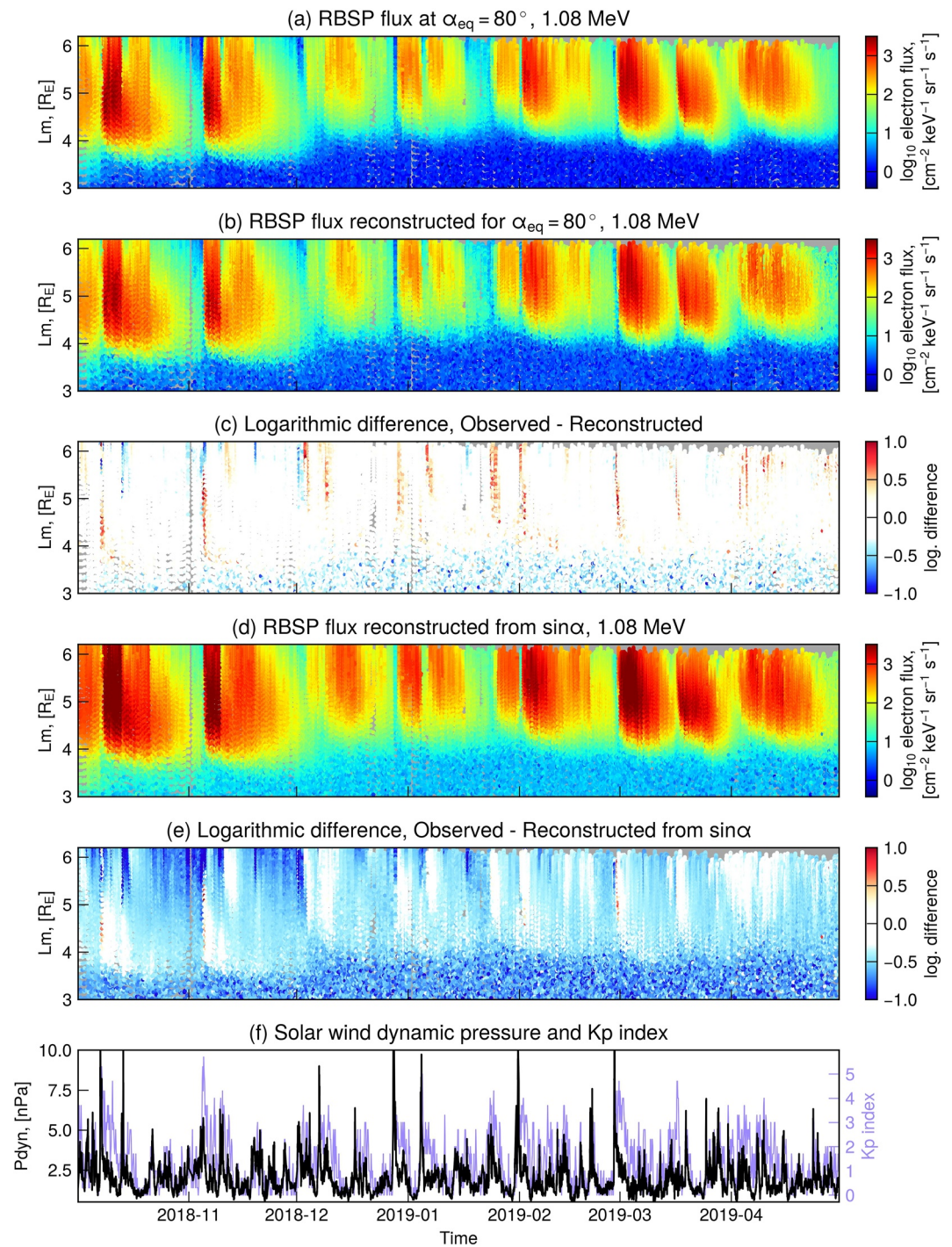
Figure 5. (a) Radiation Belt Storm Probes (RBSP) equatorial electron flux for 1.08 MeV, (b) RBSP equatorial flux reconstructed from two lowest Magnetic Electron Ion Spectrometer (MagEIS) pitch angles using the developed pitch angle distribution model, (c) logarithmic difference between observed and propagated flux; (d) equatorial electron flux propagated using the $\sin(\alpha)$ approximation, (e) logarithmic difference between observed flux and the propagated one, (f) solar wind dynamic pressure.

improvement in performance by the Fourier expansion compared to $\sin(\alpha)$, we calculated the skill score, given by the formula:

$$SS = 1 - \frac{\sum_{i=1}^{N}(m_i - o_i)^2}{\sum_{i=1}^{N}(b_i - o_i)^2},\tag{8}$$

where m denotes the model values, o stands for observations, and b represents the baseline model output. This metric quantifies the improvement over a baseline model, and is also sometimes referred to as the prediction efficiency (PE) (for details see e.g., Glauert et al., 2018; Morley et al., 2018). In our case, the skill score equals 93%, meaning that the proposed approximation and modeling of the PADs is strongly beneficial compared to the standard simplified approach.

4.2. Reconstructing Equatorial PADs From a Single Flux Measurement

In order to reconstruct the equatorial electron PADs from a single measurement, be that a uni- or omni-directional one, it is necessary to create a model of the A0 coefficient. Here, we parametrize the A0 in each L-MLT bin (the binning procedure remains the same as before) as a function of the solar wind velocity. The A0 coefficient essentially represents a value of flux in the edge of the loss cone. It should be noted, however, that due to the fact that RBSP did not have a high resolution in the loss cone, the A0 value is not a physical parameter but rather an artificial value from the details of the measurement that averages the zero intensity loss cone together with the finite intensities at small pitch angles. It has been well established that changes in electron flux are related to the solar wind velocity which is why we use this quantity here instead of the otherwise used pressure (Reeves et al., 2011). It has also been noted that solar wind velocity is one of the most meaningful predictor variables for empirical flux modeling (e.g., Katsavrias et al., 2022; Li et al., 2005; Sillanpää et al., 2017; A. Smirnov, et al., 2020; Wing et al., 2016). For relativistic electrons, Reeves et al. (2011) reported that the distribution of flux versus SW velocity resembled a triangle. Kellerman and Shprits (2012) analyzed the normalized occurrence histograms of electron flux observations at GEO with respect to the solar wind velocity and reported a well-observed non-linear trend between them. In the present study, a similar normalization procedure is used, namely, for each bin of solar wind velocity we compute the normalized distribution of electron flux. In Figure 6, we show the normalized occurrence histograms of the A0 in logarithmic scale on solar wind velocity for two energies (142 keV and 1.08 MeV) and day and night MLT sectors with L > 5.7. One can observe a strong dependence of A0 on Vsw. While for the lower energies this dependence has a quadratic shape, for 1.08 MeV electrons the trend appears linear.

In case of a single uni-directional measurement, Equations (5) and (7) can be applied in combination with an appropriate model of the A0 coefficient. Furthermore, if the flux measurement is locally omnidirectional, the model PAD can be integrated from 0° up to the maximum equatorial PA, and the scaling factor can be retrieved through the same relation. It should be noted that the A0 model used here is very simple, as it is well known that the solar wind velocity cannot fully explain the variability of flux in the radiation belt region (e.g., Reeves et al., 2011). For instance, during quiet times the flux intensities can be lower than the averaged A0 value predicted using this simple model. This would cause unphysical PAD shapes. To avoid this, the value of the observed flux at α_0 needs to be higher than A0. The entries where this does not hold are removed from the analysis. The reconstructions shown here use the PA value of 20°. The main interest in such formulation lies in retrieving PADs from the omni-directional data for MEO constellations such as GPS. Within the range of L-shells covered by our model (3–6), GPS pitch angles vary from 90° to approximately 35–40°, and the assumption on the selected PA holds most of the time.

Figure 7 shows an example of the model reconstruction for the 142 keV electron flux. Similar to Figure 5, in Figure 7(a) we show the RBSP flux during the test interval. In panel (b) the flux reconstructed using the A0 model and the proposed pitch angle model is demonstrated. Their logarithmic difference is shown in Figure 7(c). It is evident that the model performs well in the outer zone, as the difference between model predictions and observations is close to zero. At the same time, a significant portion of the data in the inner zone and slot region is removed during the flux reconstruction. This is likely due to the simplicity of the A0 model we used here. The slot region corresponds to highly complex dynamics, including slot filling events, that are not expected to be captured by a flux model which depends only on solar wind velocity and does not use time history. It should
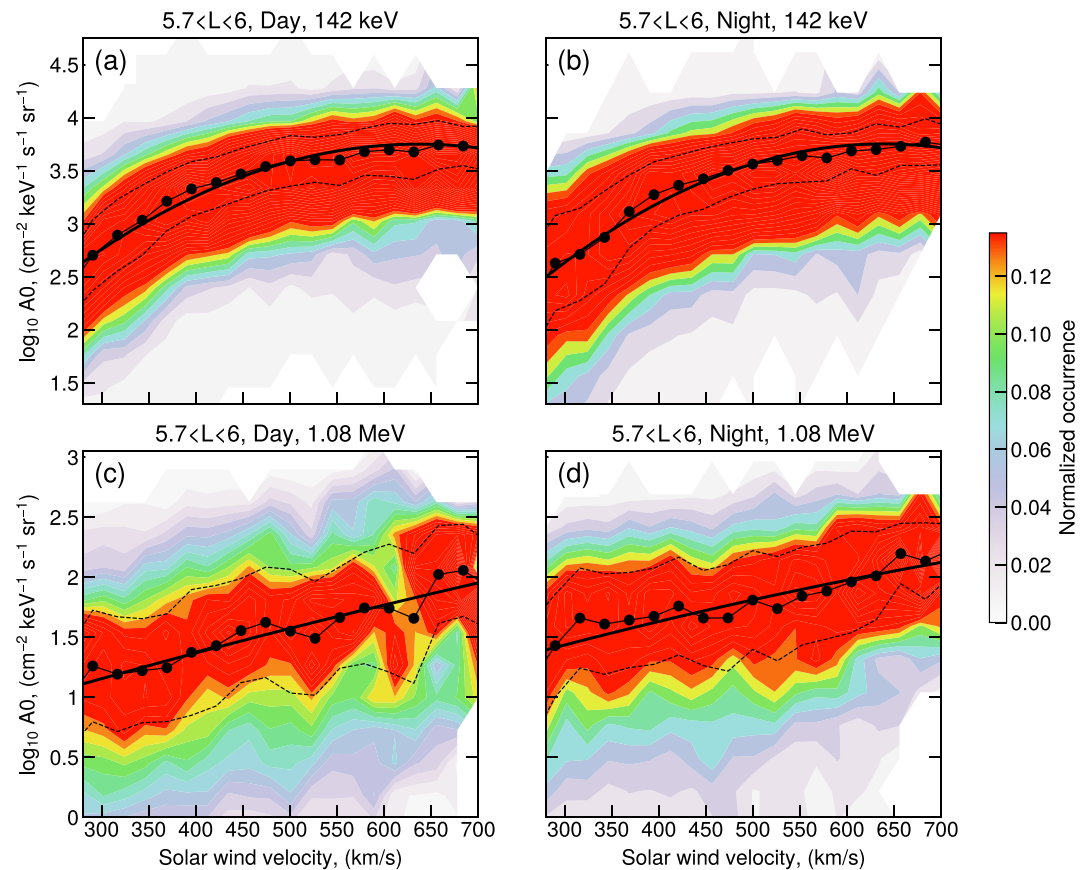
Figure 6. Normalized occurrence plots of the A_0 coefficient as a function of solar wind velocity for 142 and 1.08 MeV electrons at day side magnetic local time (MLT) (a,c) and night side MLT (b,d), respectively. The median A0 values in each velocity bin are shown as black dots, and the dashed lines give the interquartile range. The bold black line shows the quadratic trends fitted to the medians.

be noted that at L<4, there is an overestimation of the inner zone fluxes by the model, however it is smaller than for the reconstructions based on $\sin(\alpha)$ function (-0.33 compared to -0.5 in logarithmic scale). Therefore, even though the flux reconstructions based on the A0 model remove most of the points in the slot region, the technique described in this subsection gives good accuracy in the outer belt with an overall skill score of 39% over the standard $\sin(\alpha)$ approximation.

5. Discussion

Electron PADs are of paramount importance for understanding the physical processes acting in the Earth's radiation belts and ring current. Observations in the vicinity of the geomagnetic equator yield the most complete information about the electron PADs, and the equatorial PADs are also indicative of the processes in other parts of the inner magnetosphere. For example, at an off-equatorial latitude a PAD sampled by a satellite can be retrieved by taking a part of the corresponding equatorial PAD from 0° to the maximum equatorial PA corresponding to the satellite location. The inverse, however, does not hold - it is physically impossible to reconstruct the full equatorial PAD only having observations at high latitudes. However, that information can still be filled in through independent sources as the empirical model that we provide here.

In this study we analyzed electron PADs at energies 30 keV–1.6 MeV in the outer belt. It has been demonstrated that the PADs can be well approximated by a combination of the first, third and fifth sine harmonics. We create an empirical model of the PAD shapes in terms of the respective coefficients, driven by the solar wind dynamic pressure. We have also examined the probability distributions of the PAD shape coefficients (A1, A3 and A5) with
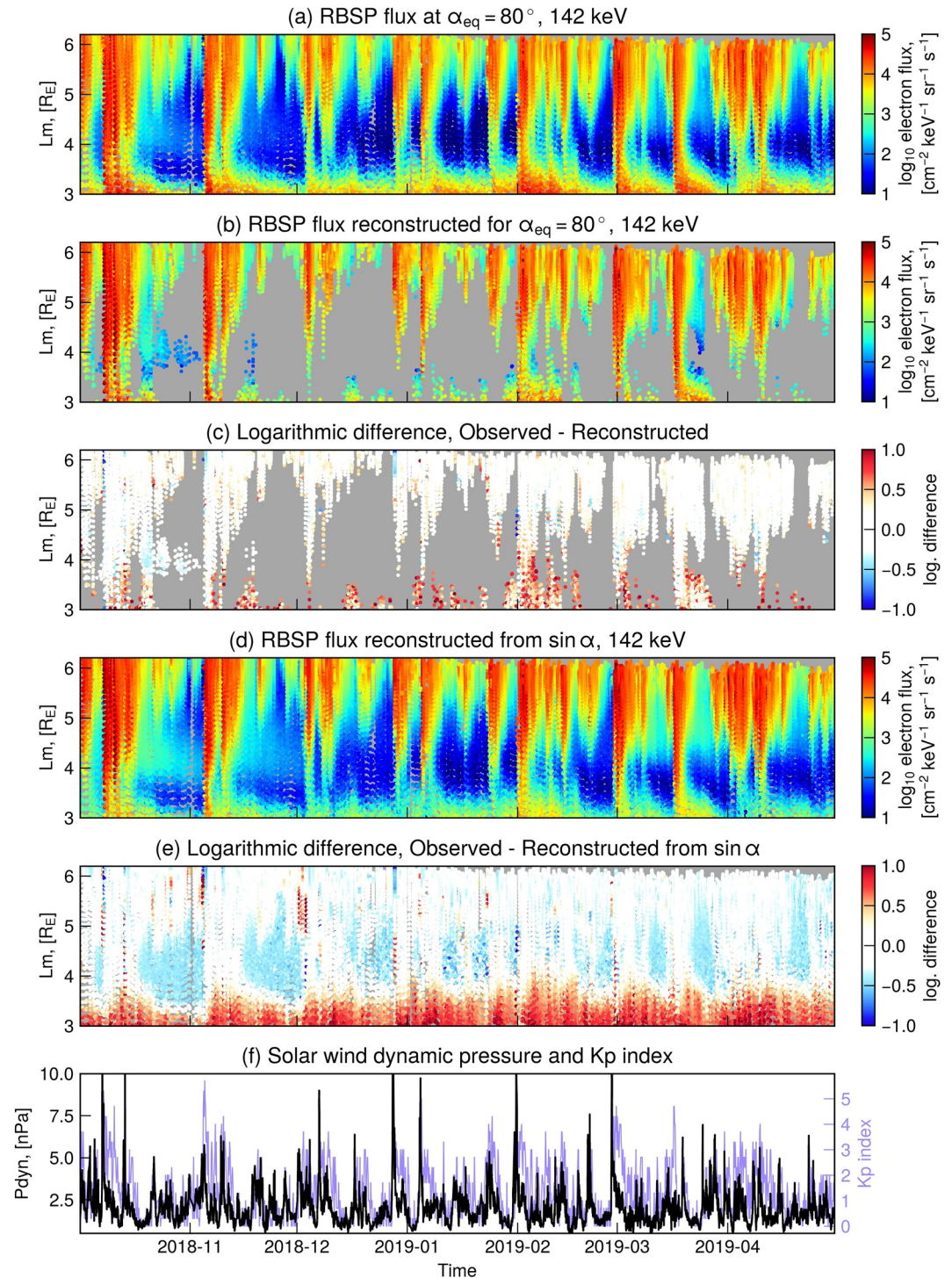
Figure 7. Same as Figure 5, but for a single uni-directional observation and the A0 model used for flux reconstruction.

respect to the Auroral Electrojet (AE) and SYM-H indices, as well as several solar wind parameters (velocity, By and Bz components of the interplanetary magnetic field). It was found that of the considered proxies the dynamic pressure was the best parameter to capture the PAD dynamics with increasing activity, while other parameters exhibited much weaker or irregular trends (see Figure S3 Supporting Information S1). Furthermore, asymmetries in the terrestrial magnetosphere can to a large extent be attributed to changes in SW pressure, and therefore we used it as a predictor variable for the model. At the same time, the A0 coefficient exhibited a strong dependence on solar wind velocity. This coefficient represents electron flux in the loss cone, and the relation of flux to SW
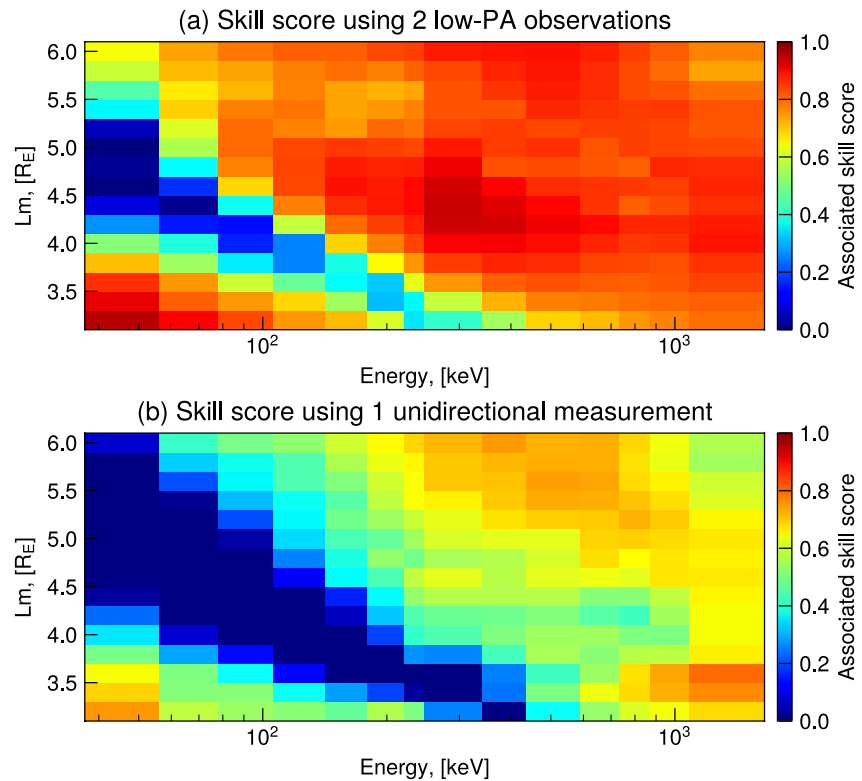
Figure 8. Associated skill score (SS) of the 80° equatorial pitch angle electron flux reconstructions using the proposed pitch angle distribution model over the simple $\sin(\alpha)$ approximation using two methods proposed in Sections 4.1 and 4.2. (a) SS of the reconstructions using two observations at low pitch angles; (b) SS of the reconstructions from a single unidirectional flux measurement.

velocity has long been established (see e.g., Reeves et al., 2011). We note, however, that the quadratic relation of A_0 to v_{sw} introduced here is very simple, and the appropriate time lag between the two, which for energies of >1 MeV can be in the order of several days, was not investigated.

Our PAD model was constructed for the normalized PAD shapes, and in order to reconstruct the equatorial electron flux values it is necessary to employ electron flux observations. We describe two techniques for flux reconstructions. The first method (Section 4.1) involves two flux observations at low equatorial pitch angles. Another method, described in Section 4.2, can be used when a single flux measurement is available and works for both uni- and omni-directional observations. It was established that the developed model outperforms the standard sine approximation. In Figure 8, we demonstrate the skill score of our PAD model over the simple propagation of flux to high PAs using the $\sin(\alpha)$ function for both methods, binned by 0.2 L for each of the MagEIS energy channels. The skill score for the first method (involving two low-PA data points) is generally very high (over 90%) at all energies and L-shells, except for the slot region where the SS values are $\sim 20\% - 50\%$. Furthermore, as shown in Figure 3, the reconstructed flux values are very close to the MagEIS observations. Therefore, the developed model can be a useful tool for highly accurate reconstructions of the equatorial flux from observations at low PAs.

In Figure 8(b), we demonstrate the skill score for the second method which involves a single flux measurement. It can be seen that at energies >∼300 keV, the model outperforms the standard approach by >50% in the outer belt. Furthermore, at lower energies the flux propagated using the $\sin(\alpha)$ is underestimated at low L-shells (as shown in Figure 7d), and therefore the skill score corresponding to the outer edge of the inner zone is generally above 50%. However, in the slot region, a significant number of points are removed during the flux reconstructions (see also Figure 7b) and the corresponding SS values are around zero and sometimes negative. This means that the second method does not lead to any improvement over $\sin(\alpha)$ extrapolation in the slot region. This is due to the fact that this approach relies on the A0 model, which as described above is rather simple and does not carry the full information about the flux variability, even more so in the slot region where the dynamics is very complex. It should be noted, however, that the statistics in the slot region are based on a much smaller number of points, and furthermore, electron flux in the slot region is

often at background levels and the performance metrics may not be appropriate in this case. The second approach presented here can be applied to reconstruct flux for energies >300 keV in the outer belt, but in order to apply this method to lower energies a more precise A0 model needs to be developed in the future. Introducing such a model will likely lead to higher SS values matching those in Figure 8(a).

6. Conclusions

Using the full MagEIS data set of pitch angle resolved electron flux at energies 30 keV - ~1.6 MeV in 2012–2019, we analyze equatorial electron PADs at $L = 3$–6. To fit the PADs, we use a combination of the first, third and fifth sine harmonics. This approximation can fit all PAD types observed in the outer radiation belt, and the coefficients before the three sine terms relate to the main PAD shapes. Furthermore, the resulting expression can be analytically integrated and the fitted PADs converted to omnidirectional flux.

We present a PAD model with a continuous dependence on L, MLT and activity parametrized by the solar wind dynamic pressure. We demonstrated that the model can be applied to reconstruct the full equatorial PADs from observations at low pitch angles, and therefore can be applied to LEO data. In particular, it can help with using the LEO observations for data assimilation (e.g., Castillo et al., 2021), for driving the boundary conditions of the physics-based simulations, and for converting these measurements to phase space density in terms of adiabatic invariants for which the correct PAD shapes are critically important (Chen et al., 2005). Moreover, the model can be applied to reconstruct the equatorial PAD from a single uni- or omnidirectional measurement. This is of particular interest for the long-term MEO constellations, for instance, the GPS constellation (Morley et al., 2018) and the Cluster mission (e.g., Kronberg et al., 2021; Smirnov et al., 2019, A. G. Smirnov et al., 2020), and would add to the availability of the PA-resolved data in the outer radiation belt region. The model can further be extended to higher L-values by using the data from the currently operating Arase constellation, already cross-calibrated with the RBSP (Szabó-Roberts et al., 2021).

Data Availability Statement

The model coefficients and the Python script to read them (Smirnov et al., 2022a) are publicly available by the link https://doi.org/10.5880/GFZ.2.7.2022.001. The pitch angle resolved Magnetic Electron Ion Spectrometer data are publicly available at https://rbsp-ect.newmexicoconsortium.org/rbsp_ect.php. The solar wind and geomagnetic indices were downloaded from the OMNIWeb database (https://omniweb.gsfc.nasa.gov). The Auroral Electrojet and SYM-H indices used in this paper were provided by the WDC for Geomagnetism, Kyoto (http://wdc.kugi.kyoto-u.ac.jp/wdc/Sec3.html). The planetary Kp index of geomagnetic activity was obtained from GFZ Potsdam (https://www.gfz-potsdam.de/en/kp-index/).

References

Albert, J. M., Starks, M. J., Horne, R. B., Meredith, N. P., & Glauert, S. A. (2016). Quasi-linear simulations of inner radiation belt electron pitch angle and energy distributions. *Geophysical Research Letters*, *43*(6), 2381–2388. https://doi.org/10.1002/2016gl067938

Allison, H. J., Horne, R. B., Glauert, S. A., & Del Zanna, G. (2018). Determination of the equatorial electron differential flux from observations at low Earth orbit. *Journal of Geophysical Research: Space Physics*, *123*(11), 9574–9596. https://doi.org/10.1029/2018ja025786

Artemyev, A., Agapitov, O., Mozer, F., & Spence, H. (2015). Butterfly pitch angle distribution of relativistic electrons in the outer radiation belt: Evidence of nonadiabatic scattering. *Journal of Geophysical Research: Space Physics*, *120*(6), 4279–4297. https://doi.org/10.1002/2014ja020865

Blake, J., Carranza, P. A., Claudepierre, S. G., Clemmons, J. H., Crain, W. R. Jr., Dotan, Y., et al. (2013). The magnetic electron ion spectrometer (MagEIS) instruments aboard the radiation belt storm probes (RBSP) spacecraft. *Space Science Reviews*, *179*, 383–421. The Van Allen Probes Mission.

Bortnik, J., Li, W., Thorne, R. M., & Angelopoulos, V. (2016). A unified approach to inner magnetospheric state prediction. *Journal of Geophysical Research: Space Physics*, *121*(3), 2423–2430. https://doi.org/10.1002/2015JA021733

Carbary, J., Mitchell, D., Paranicas, C., Roelof, E., Krimigis, S., Krupp, N., et al. (2011). Pitch angle distributions of energetic electrons at Saturn. *Journal of Geophysical Research*, *116*(A1). https://doi.org/10.1029/2010ja015987

Castillo, A. M. T., de Wiljes, J., Shprits, Y. Y., & Aseev, N. A. (2021). Reconstructing the dynamics of the outer electron radiation belt by means of the standard and ensemble kalman filter with the verb-3d code. *Space Weather*, *19*(10), e2020SW002672. https://doi.org/10.1029/2020sw002672

Chen, Y., Friedel, R. H., Henderson, M. G., Claudepierre, S. G., Morley, S. K., & Spence, H. E. (2014). Repad: An empirical model of pitch angle distributions for energetic electrons in the Earth's outer radiation belt. *Journal of Geophysical Research: Space Physics*, *119*(3), 1693–1708. https://doi.org/10.1002/2013ja019431

Chen, Y., Friedel, R. H. W., Reeves, G. D., Onsager, T. G., & Thomsen, M. F. (2005). Multisatellite determination of the relativistic electron phase space density at geosynchronous orbit: Methodology and results during geomagnetically quiet times. *Journal of Geophysical Research*, *110*(A10). https://doi.org/10.1029/2004JA010895

Clark, G., Paranicas, C., Santos-Costa, D., Livi, S., Krupp, N., Mitchell, D., et al. (2014). Evolution of electron pitch angle distributions across Saturn's middle magnetospheric region from MIMI/LEMMS. *Planetary and Space Science*, *104*, 18–28. https://doi.org/10.1016/j.pss.2014.07.004

Claudepierre, S., Blake, J. B., Boyd, A. J., Clemmons, J. H., Fennell, J. F., Gabrielse, C., et al. (2021). The magnetic electron ion spectrometer: A review of on-orbit sensor performance, data, operations, and science. *Space Science Reviews*, *217*(8), 1–67. https://doi.org/10.1007/s11214-021-00855-2

Claudepierre, S. G., & O'Brien, T. P. (2020). Specifying high-altitude electrons using low-altitude leo systems: The SHELLS model. *Space Weather*, *18*(3), e2019SW002402. https://doi.org/10.1029/2019sw002402

Gannon, J. L., Li, X., & Heynderickx, D. (2007). Pitch angle distribution analysis of radiation belt electrons based on combined release and radiation effects satellite medium electrons a data. *Journal of Geophysical Research*, *112*(A5). https://doi.org/10.1029/2005JA011565

Glauert, S. A., Horne, R. B., & Meredith, N. P. (2018). A 30-year simulation of the outer electron radiation belt. *Space Weather*, *16*(10), 1498–1522. https://doi.org/10.1029/2018sw001981

Green, J., O'Brien, T., Claudepierre, S., & Boyd, A. (2021). Removing orbital variations from low altitude particle data: Method and application. *Space Weather*, *19*(2), e2020SW002638. https://doi.org/10.1029/2020sw002638

Gu, X., Zhao, Z., Ni, B., Shprits, Y., & Zhou, C. (2011). Statistical analysis of pitch angle distribution of radiation belt energetic electrons near the geostationary orbit: Crres observations. *Journal of Geophysical Research*, *116*(A1). https://doi.org/10.1029/2010JA016052

Horne, R. B., Meredith, N. P., Thorne, R. M., Heynderickx, D., Iles, R. H. A., & Anderson, R. R. (2003). Evolution of energetic electron pitch angle distributions during storm time electron acceleration to megaelectronvolt energies. *Journal of Geophysical Research*, *108*(A1), SMP11–1–SMP11–13. https://doi.org/10.1029/2001JA009165

Kamiya, K., Seki, K., Saito, S., Amano, T., & Miyoshi, Y. (2018). Formation of butterfly pitch angle distributions of relativistic electrons in the outer radiation belt with a monochromatic Pc5 wave. *Journal of Geophysical Research: Space Physics*, *123*(6), 4679–4691. https://doi.org/10.1002/2017ja024764

Katsavrias, C., Aminalragia-Giamini, S., Papadimitriou, C., Daglis, I. A., Sandberg, I., & Jiggens, P. (2022). Radiation belt model including semi-annual variation and solar driving (sentinel). *Space Weather*, *20*(1), e2021SW002936. https://doi.org/10.1029/2021sw002936

Katsavrias, C., Aminalragia–Giamini, S., Papadimitriou, C., Sandberg, I., Jiggens, P., Daglis, I., & Evans, H. (2021). On the interplanetary parameter schemes which drive the variability of the source/seed electron population at geo. *Journal of Geophysical Research: Space Physics*, *126*(6), e2020JA028939. https://doi.org/10.1029/2020JA028939

Kellerman, A. C., & Shprits, Y. Y. (2012). On the influence of solar wind conditions on the outer-electron radiation belt. *Journal of Geophysical Research*, *117*(A5). https://doi.org/10.1029/2011JA017253

Kronberg, E. A., Daly, P. W., Grigorenko, E. E., Smirnov, A. G., Klecker, B., & Malykhin, A. Y. (2021). Energetic charged particles in the terrestrial magnetosphere: Cluster/RAPID results. *Journal of Geophysical Research: Space Physics*, *126*(9), e2021JA029273. https://doi.org/10.1029/2021JA029273

Li, X., Baker, D., Temerin, M., Reeves, G., Friedel, R., & Shen, C. (2005). Energetic electrons, 50 kev to 6 mev, at geosynchronous orbit: Their responses to solar wind variations. *Space Weather*, *3*(4). https://doi.org/10.1029/2004sw000105

Lyons, L. R., Thorne, R. M., & Kennel, C. F. (1972). Pitch-angle diffusion of radiation belt electrons within the plasmasphere. *Journal of Geophysical Research*, *77*(19), 3455–3474. https://doi.org/10.1029/ja077i019p03455

Mauk, B., Fox, N. J., Kanekal, S., Kessel, R., Sibeck, D., & Ukhorskiy, a. A. (2012). *Science objectives and rationale for the radiation belt storm probes mission* (pp. 3–27). The Van Allen Probes Mission.

Morley, S. K., Brito, T. V., & Welling, D. T. (2018). Measures of model performance based on the log accuracy ratio. *Space Weather*, *16*(1), 69–88. https://doi.org/10.1002/2017sw001669

Ni, B., Zou, Z., Gu, X., Zhou, C., Thorne, R. M., Bortnik, J., et al. (2015). Variability of the pitch angle distribution of radiation belt ultrarelativistic electrons during and following intense geomagnetic storms: Van Allen Probes observations. *Journal of Geophysical Research: Space Physics*, *120*(6), 4863–4876. https://doi.org/10.1002/2015ja021065

Ni, B., Zou, Z., Li, X., Bortnik, J., Xie, L., & Gu, X. (2016). Occurrence characteristics of outer zone relativistic electron butterfly distribution: A survey of van allen probes rept measurements. *Geophysical Research Letters*, *43*(11), 5644–5652. https://doi.org/10.1002/2016gl069350

Reeves, G., McAdams, K., Friedel, R., & O'Brien, T. (2003). Acceleration and loss of relativistic electrons during geomagnetic storms. *Geophysical Research Letters*, *30*(10). https://doi.org/10.1029/2002gl016513

Reeves, G. D., Friedel, R. H. W., Larsen, B. A., Skoug, R. M., Funsten, H. O., Claudepierre, S. G., et al. (2016). Energy-dependent dynamics of kev to mev electrons in the inner zone, outer zone, and slot regions. *Journal of Geophysical Research: Space Physics*, *121*(1), 397–412. https://doi.org/10.1002/2015ja021569

Reeves, G. D., Morley, S. K., Friedel, R. H., Henderson, M. G., Cayton, T. E., Cunningham, G., et al. (2011). On the relationship between relativistic electron flux and solar wind velocity: Paulikas and Blake revisited. *Journal of Geophysical Research*, *116*(A2). https://doi.org/10.1029/2010ja015735

Reidy, J., Horne, R., Glauert, S., Clilverd, M., Meredith, N., Woodfield, E., et al. (2021). Comparing electron precipitation fluxes calculated from pitch angle diffusion coefficients to LEO satellite observations. *Journal of Geophysical Research: Space Physics*, *126*(3), e2020JA028410. https://doi.org/10.1029/2020ja028410

Roederer, J. G. (1967). On the adiabatic motion of energetic particles in a model magnetosphere. *Journal of Geophysical Research*, *72*(3), 981–992. https://doi.org/10.1029/jz072i003p00981

Roederer, J. G., & Zhang, H. (2016). *Dynamics of magnetically trapped particles*. Springer.

Selesnick, R., & Blake, J. (2002). Relativistic electron drift shell splitting. *Journal of Geophysical Research*, *107*(A9), 1265. https://doi.org/10.1029/2001ja009179

Sen, P. K. (1968). Estimates of the regression coefficient based on kendall's tau. *Journal of the American Statistical Association*, *63*(324), 1379–1389. https://doi.org/10.1080/01621459.1968.10480934

Sillanpää, I., Ganushkina, N. Y., Dubyagin, S., & Rodriguez, J. (2017). Electron fluxes at geostationary orbit from goes maged data. *Space Weather*, *15*(12), 1602–1614. https://doi.org/10.1002/2017sw001698

Smirnov, A., Berrendorf, M., Shprits, Y. Y., Kronberg, E. A., Allison, H. J., Aseev, N. A., et al. (2020). Medium energy electron flux in Earth's outer radiation belt (merlin): A machine learning model. *Space Weather*, *18*(11), e2020SW002532. https://doi.org/10.1029/2020sw002532

Smirnov, A., Kronberg, E. A., Latallerie, F., Daly, P. W., Aseev, N., Shprits, Y. Y., et al. (2019). Electron intensity measurements by the Cluster/RAPID/IES instrument in Earth's radiation belts and ring current. *Space Weather*, *17*(4), 553–566. https://doi.org/10.1029/2018sw001989

Smirnov, A., Shprits, Y., Allison, H., Aseev, N., Drozdov, A., Kollmann, P., et al. (2022a). An empirical model of electron pitch angle distributions in the outer radiation belt based on Van Allen Probes data. V. 1.1. *GFZ Data Services*. https://doi.org/10.5880/GFZ.2.7.2022.001

Smirnov, A., Shprits, Y., Allison, H., Aseev, N., Drozdov, A., Kollmann, P., et al. (2022b). Storm-time evolution of the equatorial electron pitch angle distributions in Earth's outer radiation belt. *Frontiers in Astronomy and Space Sciences*, *9*. https://doi.org/10.3389/fspas.2022.836811

Smirnov, A. G., Kronberg, E. A., Daly, P. W., Aseev, N. A., Shprits, Y. Y., & Kellerman, A. C. (2020). Adiabatic invariants calculations for cluster mission: A long-term product for radiation belts studies. *Journal of Geophysical Research: Space Physics*, *125*(2), e2019JA027576. https://doi.org/10.1029/2019ja027576

Szabó-Roberts, M., Shprits, Y. Y., Allison, H. J., Vasile, R., Smirnov, A. G., Aseev, N. A., et al. (2021). Preliminary statistical comparisons of spin-averaged electron data from Arase and van allen probes instruments. *Journal of Geophysical Research: Space Physics*, e2020JA028929.

Theil, H. (1950). A rank-invariant method of linear and polynomial regression analysis. *Indagationes Mathematicae*, *12*(85), 173.

Tsyganenko, N., & Sitnov, M. (2005). Modeling the dynamics of the inner magnetosphere during strong geomagnetic storms. *Journal of Geophysical Research*, *110*(A3). https://doi.org/10.1029/2004ja010798

Vampola, A. (1998). Outer zone energetic electron environment update. In *Conference on the high energy radiation background in space. Workshop record* (pp. 128–136). IEEE.

Van Allen, J. A., & Frank, L. A. (1959). Radiation around the Earth to a radial distance of 107, 400 km. *Nature*, *183*(4659), 430–434. https://doi.org/10.1038/183430a0

Walt, M. (2005). *Introduction to geomagnetically trapped radiation*. Cambridge University Press.

West, H., Buck, R., & Walton, J. (1973). Electron pitch angle distributions throughout the magnetosphere as observed on Ogo 5. *Journal of Geophysical Research*, *78*(7), 1064–1081. https://doi.org/10.1029/ja078i007p01064

Wing, S., Johnson, J. R., Camporeale, E., & Reeves, G. D. (2016). Information theoretical approach to discovering solar wind drivers of the outer radiation belt. *Journal of Geophysical Research: Space Physics*, *121*(10), 9378–9399. https://doi.org/10.1002/2016ja022711

Zhao, H., Friedel, R. H. W., Chen, Y., Baker, D. N., Li, X., Malaspina, D. M., et al. (2021). Equatorial pitch angle distributions of 1–50 keV electrons in Earth's inner magnetosphere: An empirical model based on the van allen probes observations. *Journal of Geophysical Research: Space Physics*, *126*(1), e2020JA028322. https://doi.org/10.1029/2020ja028322

Zhao, H., Friedel, R. H. W., Chen, Y., Reeves, G. D., Baker, D. N., Li, X., et al. (2018). An empirical model of radiation belt electron pitch angle distributions based on Van Allen Probes measurements. *Journal of Geophysical Research: Space Physics*, *123*(5), 3493–3511. https://doi.org/10.1029/2018ja025277